



Micromorphology and microtexture evaluation of poly(*o*-ethoxyaniline) films using atomic force microscopy and fractal analysis

Ricardo Messias Ito¹ · Cindel Cavalcante de Souza¹ · Ariamna María Dip Gandarilla² · Larissa Medeiros de Oliveira³ · Walter Ricardo Brito² · Edgar Aparecido Sanches³ · Robert Saraiva Matos^{4,5} · Henrique Duarte da Fonseca Filho¹

Received: 8 June 2020 / Accepted: 17 August 2020 / Published online: 8 September 2020
© The Polymer Society, Taipei 2020

Abstract

The morphology and microtexture of poly(*o*-ethoxyaniline) thin films deposited on the ITO substrate by electrodeposition were investigated. Cyclic voltammetry and FTIR were used to characterize the molecular structure, while Atomic Force Microscopy (AFM) technique was applied to obtain topographical images. The images were analyzed using commercial and free software. Moreover, three new parameters such as surface entropy, fractal succolarity, and fractal lacunarity were evaluated using recently developed theoretical models. The results showed that the morphology was affected according to the deposition cycles, while the analysis of the molecular structure indicated an increase in the polymer's conjugation, mainly from 5 to 15 cycles. Structures related to the growth of poly(*o*-ethoxyaniline) were observed due to the increase in the number of deposition cycles. However, films did not grow completely. The microtexture was homogenized as the number of cycles increased. Furthermore, topographical uniformity was high for all films. Percolation remained low for all films, showing that although the formation of films was not completed, the microtexture of the material tended to homogenize as the film grew. These results revealed that the used tools can quantify the surface parameters, which are of great interest for the study of the corrosive properties of polymeric thin films.

Keywords Poly(*o*-ethoxyaniline) films · Atomic force microscope · Fractal analysis · Roughness · Topology

Introduction

Conjugated polymers represent a special group of materials widely studied and applied in various scientific and technological research [1], such as biomedical engineering [2],

chemical or biological sensors [3–5], catalysis or electrocatalysis [6, 7], energy storage devices [8, 9] and anti-corrosion coatings [10–12]. Among conjugated polymers, polyaniline (PANI) and its derivatives have been attracting significant interest due to its high conductivity, environmental stability, easy obtaining process, low cost of raw materials, and interesting technological applications [8, 13, 14]. Bilal et al. verified that ring-substituted PANI derivatives can protect metals against corrosion [15]. Several routes of synthesis using polymerization techniques in the aqueous and non-aqueous medium have been proposed considering the variation of several parameters such as pH, oxidizing agents, reactants concentration, temperature, time, and polymerization conditions [16].

Poly(*o*-ethoxyaniline) (POEA) is a derivative of PANI and its structural difference is the presence of the group (–OCH₂CH₃) in the ortho position of the aniline rings [17]. POEA can be obtained by different synthesis methods, including chemical [18–21] and electropolymerization [2, 22]. Nanofibers, nanorods, nanotubes, nanoflakes, and nanospheres [23, 24] have been obtained in chemical

✉ Henrique Duarte da Fonseca Filho
henriquedffilho@yahoo.com.br

¹ Laboratory of Synthesis of Nanomaterials and Nanoscopy, Physics Department, Federal University of Amazonas-UFAM, Manaus, Amazonas, Brazil
² Laboratório de Bioeletrônica e Eletroanalítica (LABEL), Department of Chemistry, Federal University of Amazonas, Manaus, Amazonas 69067-005, Brazil
³ Laboratório de Polímeros Nanoestruturados (NANOPOLO) – @nanopol_ufam UFAM, Manaus/AM, Brazil
⁴ Amazonian Materials Group, Physics Department, Federal University of Amapá-UNIFAP, Macapá, Amapá, Brazil
⁵ Postgraduate Program in Materials Science and Engineering, Federal University of Sergipe-UFS, São Cristóvão, Sergipe, Brazil

polymerization using different oxidants or additives. On the other hand, the electrochemical polymerization represents a simple method of consuming less energy, besides the resulting film morphology can be controlled by varying the deposition experimental conditions [25–27]. The influence of substituent in the ortho-position of aniline ring can influence on the polymerization process, decreasing the molar mass of the polymer and requiring longer polymerization time. Furthermore, the steric and electronic effects of aniline substituent influence the electrical conductivity [19, 28].

Aiming at using conjugated polymers as corrosion surface protectors, the formed film must present high strength, good chemical stability, as well as wear resistance. Chaudhari et al. synthesized strongly adherent POEA coatings on copper substrates by electrochemical polymerization of *o*-ethoxyaniline in aqueous salicylate solution by using cyclic voltammetry and verified the efficient ability of these coatings as corrosion protective coatings [29]. The evaluation of the corrosion protection performance of POEA coated copper by electrochemical impedance spectroscopy has also been reported [30, 31].

Surface roughness is an important factor to be considered both for thin films or as corrosion coatings, and it is significantly influenced by several factors, including deposition parameters and type of substrate. Cena et al. [32], reported differences in the morphological characterization of thin films of polyaniline alternated with natural rubber, result that can be modified adjusting the PANI solution's pH. To date, fractal theory [33, 34] and statistical methods [35, 36] have been used to investigate surface morphology because roughness influences other surface properties such as tribology [37], wettability, and hydrophobicity [38, 39]. According to Sedláček, the main used parameters for roughness evaluation [root mean square (S_q), average roughness (S_a), skewness (S_{sk}) and kurtosis (S_{ku}), do not generate enough information [40] considering patterning, spatial distribution, and fractals of surface morphology [41, 42]. Using fractal geometry [43–45], Mandelbort [46] presented a quantitative parameter describing the surface, as well as its irregularities.

Atomic Force Microscopy (AFM) has been widely used for the evaluation of conducting polymers, allowing information about the structure and organization of thin films, surface morphology, nanostructure, packing and conformation of polymer chains, porosity, force profiles of specific chemical interactions, roughness and mapping of electrical charge [20, 47, 48]. However, the AFM technique presents some advantages, such as no need for recovering conductive samples nor the use of a vacuum system. For this reason, this technique can be applied to any material and allows simultaneous detection of phase image and height [49]. The AFM technique was carried out in this present work to evaluate the morphology and microtexture of POEA films obtained by electropolymerization. The influence of the electrodeposition number cycles was evaluated and new parameters (surface

entropy, fractal succolarity, and fractal lacunarity) were obtained using image processing. Additionally, Cyclic Voltammetry and Fourier Transform-Infrared (FTIR) spectroscopy were performed to monitor the production of the films and characterize their molecular structures.

Materials and methods

Chemicals and reagents

All reagents were of analytical grade. The *o*-ethoxyaniline (OEA) monomer was purchased from Fluka and double-distilled under reduced pressure. Acetone and isopropyl alcohol were purchased from Synth (Brazil). Sulfuric acid (98%) was purchased from Merck (Germany). Aqueous solutions were prepared by using purified water from a Milli-Q system.

POEA electrodeposition on ITO electrodes

All electrochemical procedures were performed using an AUTOLAB PGSTAT 204 (Metrohm Autolab, Netherlands), controlled with NOVA 2.1.2 electrochemical analysis software. A conventional three-electrode system was used with an indium tin oxide electrode (ITO) coated on glass substrates ($15 \Omega/\text{sq.}$, Lumtech) as the working electrode, Ag/AgCl as the reference electrode (sat. KCl), and platinum as the auxiliary electrode. The deposition area was delimited to $0,25 \text{ cm}^2$ using an insulating adhesive tape coating. All experiments were performed at room temperature without stirring. To improve the reproducibility of the measurements and obtain a good deposition, ITO substrates were ultrasonically cleaned (Q3350 ultrasonic bath, QUIMIS) in deionized water, acetone, and isopropyl alcohol, successively, for 15 min [50]. Afterward, the electrodes were dried using a nitrogen gas stream.

The POEA electrodeposition was carried out in a 0.2 mol L^{-1} OEA and 1.5 mol L^{-1} H_2SO_4 solution, using cyclic voltammetry from -0.2 to $+1.2 \text{ V}$ at a scan rate of 50 mV s^{-1} [2]. Figure 1 shows the characteristic behavior of cyclic voltammograms for the electropolymerized POEA on the ITO substrate. In this work, 4 samples were electropolymerized with 5, 15, 20, and 25 cycles, respectively, to evaluate the morphology of the different film, besides the ITO substrate. Therefore, 5 samples were labeled as #1, #2, #3, #4, and #5, where the first one was considered as the clean substrate. Finally, the samples were removed from the electrolyte solution, washed using distilled water, dried in air, and submitted to further analysis.

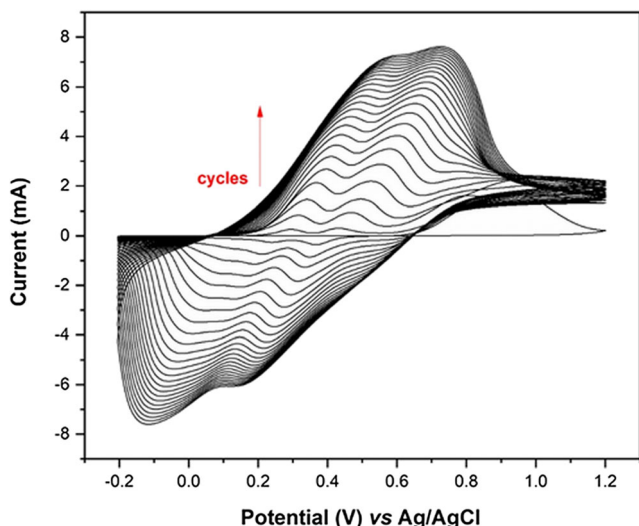


Fig. 1 Cyclic voltammograms for the electropolymerized POEA in 0.2 mol L⁻¹ OEA and 1.5 mol L⁻¹ H₂SO₄ solution

FTIR analysis

Fourier Transform-Infrared spectra were acquired using a FTIR-Nicolet 6700 (Thermo Scientific). The films were mounted on an attenuated total reflectance (ATR) accessory equipped with ZnSe crystal prior to scanning. The spectra were obtained with an accumulation of 100 scans and with a resolution of 4 cm⁻¹.

AFM imaging

An Innova AFM from Bruker (Santa Barbara, CA, USA) operated on a tapping mode was used for structural characterization. A scan rate of 0.5 Hz was used, and the size of the generated images was 5 × 5 μm² at a resolution of 256 × 256 pixels using a silicon cantilever. The feedback control to obtain the best possible images was adapted to each surface and for all the applied scans. All measurements were performed in air, at room temperature (296 ± 1) K and (40 ± 1) % relative humidity. AFM images were analyzed using the MountainsMap Premium software trial version 8.4.8872 [51], according to ISO 25178-2:2012 [52].

Roughness parameters

AFM images were analyzed using the WSxM 5.0 version software (Nanotec Eletronica S. L.) [53]. The most relevant parameters were determined by the software, such as average roughness (S_a), root mean square roughness (S_q), surface skewness (R_{sk}), and surface kurtosis (R_{ku}), using the following equations:

$$S_a = \iint |Z(x,y)|.dx.dy \tag{1}$$

$$S_q = \sqrt{\iint |Z(x,y)|^2 .dx.dy} \tag{2}$$

$$R_{sk} = \frac{\sqrt{\iint_a |Z(x,y)|^3 .dx.dy}}{\sqrt{\iint_a |Z(x,y)|^2 .dx.dy}^3} \tag{3}$$

$$R_{ku} = \frac{\sqrt{\iint_a |Z(x,y)|^4 .dx.dy}}{\sqrt{\iint_a |Z(x,y)|^2 .dx.dy}^4} \tag{4}$$

where Z(x,y) is the height function of the vertical profile [54].

Topographic homogeneity

Surface entropy used in the analysis of topographical uniformity is a new superficial statistical parameter previously discussed by Matos et al. [55]. This parameter determines the uniformity of the height distribution of the topographical profile of the films based on Shannon’s entropy. The AFM images provided a 256 × 256 binary matrix associated with the image pixels. This matrix was then inserted into Shannon’s matrix equation, described by Nosonovsky as [56]:

$$H^{(2)} = -\sum_{i=1}^N \sum_{j=1}^N p_{ij} .log p_{ij} \tag{5}$$

where p_{ij} is the probability of having or not discrepant pixels in the universe at heights.

This model also considers the normalization of entropy. For this, a boxplot defines that the non-uniform height standards would be 0 and the uniform standards 1. The pixels whose values were 0 were considered non-accessible and the others were accessible. Normalization was determined by the standardization equation proposed by Matos et al. [55]:

$$H_{matr\ alt} = \frac{H^{(2)} - H_{min}^{(2)}}{H_{max}^{(2)} - H_{min}^{(2)}} \tag{6}$$

where H_{max}⁽²⁾ represents the surface with minimum uniform patterns and H_{min}⁽²⁾ represents the non-uniform pattern surface. We focus on H_{max}⁽²⁾ values that were represented by the H symbol. The model was developed in the R language using the free software Rstudio [57] (For more details see [55]).

Fractal parameters analysis

An object that behaves like fractal has its fractal parameters well set to a fractal dimension (FD) value. The surface texture

of an object is related to the its fractal geometry [46]. However, different objects can have the same texture, but different fractal dimensions [58]. In this research, the fractal dimension evaluated the complexity of the thin films, while providing a qualitative analysis of the texture homogeneity. For this reason, two other new parameters were measured and discussed to complement the fractal dimension. FD was measured using the free software Gwyddion 2.55 [59].

The first parameter is known as fractal succolarity (FS). This parameter defines the connectivity and intercommunication of the surface with a fluid medium through a mathematical model that determines the possible direction of fluid entrance through the analyzed topography. It is known as surface percolation [60]. To determine this parameter, the model of Talu et al. [61] was employed. This model considers the same matrix used in the calculation of surface entropy. The average value of the distribution of heights was determined as a way of defining a limit value. The values below are named 0 and above 1; pixels accessible to water have a value of 0 and pixels inaccessible 1. After some computational routines, the FS values were calculated according to Melo and Conci equation [60]:

$$FS(T(k), dir) = \frac{\sum_{k=1}^n P_0(T(k)) \cdot PR(T(k), p_c)}{\sum_{k=1}^n PR(T(k), p_c)} \quad (7)$$

where *dir* is the water inlet direction, T(k) is boxes of equal sizes T(n), P₀(T(k)) is the occupation percentage, PR is the occupation pressure, and p_c is the centroid's position (x, y) of pressure applied to the calculated box. The model also was developed in the R language, using the free software Rstudio [57].

Fractal lacunarity (FL) is a parameter that directly quantifies texture homogeneity [58]. It is a parameter that divides the image into a certain number of boxes, within which the number of gaps is calculated. Initially, it is worth explaining that this parameter is sensitive to scale, unlike the fractal dimension. The lacunarity must decrease depending on the size of the box for the object to be considered fractal. The measurements of this parameter were obtained according to the model proposed by Salcedo et al. [62]. Again, the same binary matrices extracted from the AFM images were used. The model was developed in the Fortran 77 language and compiled using the free software Force 2.0 [63]. After some computational routines recently described by Talu et al. [61], the power-law developed by Lucena and Storic [64] was applied.

$$L(r) = \alpha \cdot r^\beta \quad (8)$$

where L(r) is lacunarity, α, an arbitrary constant, and r is the box size. The exponent β can be estimated as the angular coefficient of the log (r) versus log [L(r)] curve. A

displacement of 1 was applied to the curve because the values obtained for the lacunarity were small.

Results and discussion

FTIR analysis

Analysis of FTIR spectra basically showed the absorption bands corresponding to the molecular structure of POEA. Figure 2 shows the FTIR spectra of POEA electropolymerized using 5, 10, 15, 20 and 25 cycles. The band located at 2361 cm⁻¹ was related to the angular deformation of the functional group –OCH₂CH₃ located at the *ortho* position of the carbon rings [65]. The band at ~1165 cm⁻¹ was attributed to a plane bending vibration of C–H [29]. The absorptions at 1579 and 1421 cm⁻¹ were assigned to the quinoid and benzenoid rings, respectively [29, 65]. The band at ~1022 cm⁻¹ was attributed to the 1–4 substitution on the benzene ring [29]. Finally, the bands between 800 and 700 cm⁻¹ revealed the occurrence of the 1–3 substitutions [29]. From 5 to 15 cycles, spectra indicate an decrease of the intensity of the absorption band at 1421 cm⁻¹ associated with the benzenoid vibration, as well as an increase of the intensity of the absorption band at 1579 cm⁻¹ associated with –C = C– bands of vibration. Furthermore, a red shift of the band located at 1165 cm⁻¹ assigned to the plane bending vibration of C–H was observed. From 20 to 25 cycles the intensities and position of the bands did not change considerably. These results may suggest the increase of POEA conjugation when the number of the electropolymerization cycles increased, being more evident from 5 to 15 cycles.

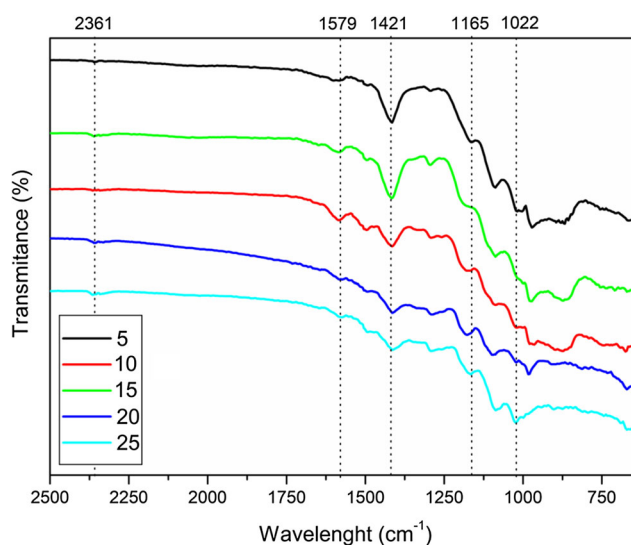


Fig. 2 FTIR spectra of POEA films

AFM measurements analysis

The surface of a material is the region more reactive than the bulk. It is the region where most of the reactivity phenomena occur. The protection of surfaces against degradation by either corrosive or erosive agents must consider the morphology and uniformity of the surface parameters. Figure 3 shows the AFM images of the used substrate and the thin films deposited by electrodeposition as a function of the number of cycles.

These images revealed that the number of cycles affected the surface morphology. While substrate #1 presented a small peak surface, from #2 to #5, the rough peaks were larger. The microstructure observed for ITO in Fig. 3a was similar to that presented by Noppakudrittidej et al. [66]. The growth of the

thin film occurred gradually, but not completely for the number of applied cycles. However, previously, Leite et al. [67] reported that these rugged peaks are conductive islands associated with the crystalline part of the POEA. These islands were observed in all samples. This is in accordance with the evolution of the polymer conjugation previously observed in the evaluation of the molecular structure of POEA discussed in section 3.1.

The coalescence of the smaller grains, formed initially due to the electrolytic process, started from #4 and continued at #5, as can be seen in Fig. 3d and e. This observation was also made previously by Mello et al. [21]. Despite the morphology presenting typical structures of POEA, many vacancies were observed, which are related to the growth process of the film

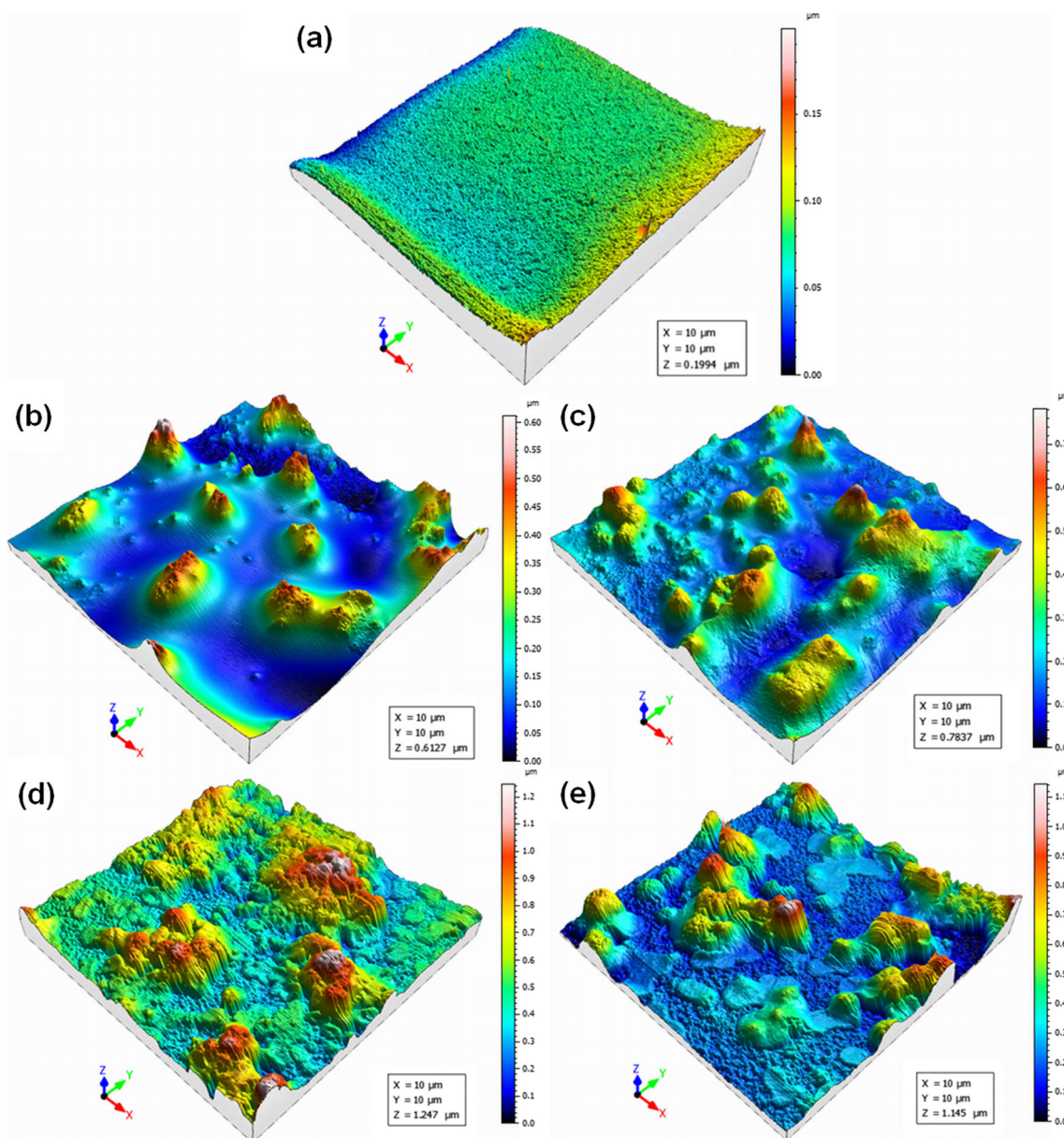


Fig. 3 Relevant 3-D AFM micrographs of samples: a #1, b #2, c #3, d #4, and e #5

[20]. Associated with the growth of the film, the surface roughness also gradually increased as a function of the number of cycles, as shown in Table 1.

The lowest roughness was recorded for substrate #1 and this is following the results found in previous works [20, 68, 69]. The highest roughness was observed for #5 (233 nm), which was also following the values reported for chitosan based-films [70]. The increase of roughness was confirmed for both S_a and S_q roughness, respectively. This phenomenon can be also attributed to the growth of the film by the coalescence of the smaller particles.

The values of asymmetry (R_{sk}) and kurtosis (R_{ku}) were higher for substrate #1, as shown in Table 1. This shows that the height distribution of the substrate was very asymmetric and leptokurtic. The films height distribution presented positive asymmetry values and close to zero (#2 to #5). This asymmetry revealed that the height distribution was practically homogeneous for all samples. However, all films also showed a leptokurtic pattern, since kurtosis was greater than 3 [71]. Platykurtic patterns may be visualized perhaps if the growth of the film was completed.

Surface microtexture

The furrows generated by the topographical profile and the contour lines generated by the particles of the films are represented in Fig. 4. Certainly, this is an interesting qualitative aspect of the surface microtexture obtained from the MountainsMap software. These images can provide a qualitative presentation of the surface microtexture through the furrows [61]. Figure 4a shows the microfurrows generated for the substrate surface. Some regions appeared with the presence of deeper channels at the bottom. The contour lines in Fig. 4f revealed how the surface was followed by differences between peaks and valleys.

Figure 4b–e revealed that the difference between peaks and valleys was strongly affected by the cycle number. Considering smaller cycles, as in #2 and #3, the particles agglomerated revealing large furrows. For larger cycles, there

was a more uniform distribution. This arrangement of the furrows showed that coalescence promoted the casting of particles into more uniform structures. Theoretically, the appearance of these evenly distributed microchannels can make it difficult for fluids to penetrate the sample. This fact can be associated with the possibility of protection against corrosive agents.

The photosimulations shown in Fig. 4g, j presented a simulation of the behavior of the particles on the surface of the thin films. For lower cycles, the particles were coalescing (regions highlighted in blue). On the other hand, for higher cycles, the particles were already more fused. In combination with the topographical images in Fig. 4d, e, the peaks suffered a flattening for these higher cycles (#4 and #5). This is probably a result of particle coalescence.

The quantitative parameters associated with the furrows are shown in Table 2. The maximum depth of the furrows increased according to the increase of the number of cycles. Higher cycles resulted in maximum depths twice that of lower cycling. The difference between peaks and valleys for these films was greater because the number of particles that did not complete the coalescence was smaller. Besides, the average depth of the furrows also increased due to the increase in the number of cycles, showing that this difference is not just an observation of the extreme values. The average furrow density, in turn, was higher for the substrate, while higher cycles resulted in films with higher furrow density per area.

The texture distribution of the films is shown in Fig. 5. Textures presenting more random distribution exhibited a strongly isotropic behavior. This occurs more for controlled surfaces than for real ones, which are generally anisotropic [72], such as wood [73]. Isotropy was lower for the substrate than any film. Figure 5a revealed that the texture presented a very random distribution, which was due to the great difference between the peaks and valleys.

Figure 5e shows that after 25 cycles the texture behaved more organically than at lower cycling. However, when we combined these results with the data in Table 3, the most isotropic behavior occurred for #2 and the most anisotropic for #4. Anisotropy does not necessarily mean that the material has a homogeneous texture. Materials whose texture can be adjusted according to a preferred direction can be of great interest as corrosive protectors.

Texture directions allowed to evaluate sensible directions. Samples #2 and #3 exhibited preferred directions at small angles (0.006748° and 0.003731°) for the third direction. However, for samples #4 and #5, these values were lower (0.006948° and 0.01703°) for the first direction. This change can be associated with the process of crystallization of the material by the coalescent phases. According to Heshmati et al. [74], phase coalescence in a polymer is divided into static and dynamic processes.

Table 1 Main superficial parameters, S_a , S_q , R_{sk} , and R_{ku} . The average results were expressed as mean value and standard deviation

Sample	Parameter			
	S_a (nm)	S_q (nm)	R_{sk}	R_{ku}
#1	5 ± 3	8 ± 3	9 ± 6	232 ± 182
#2	107 ± 11	134 ± 16	0.7 ± 0.5	3.4 ± 0.6
#3	114 ± 19	144 ± 20	1.0 ± 0.4	3.7 ± 0.8
#4	181 ± 31	227 ± 27	0.9 ± 0.4	4 ± 2
#5	190 ± 21	233 ± 20	0.9 ± 0.4	3.2 ± 0.8

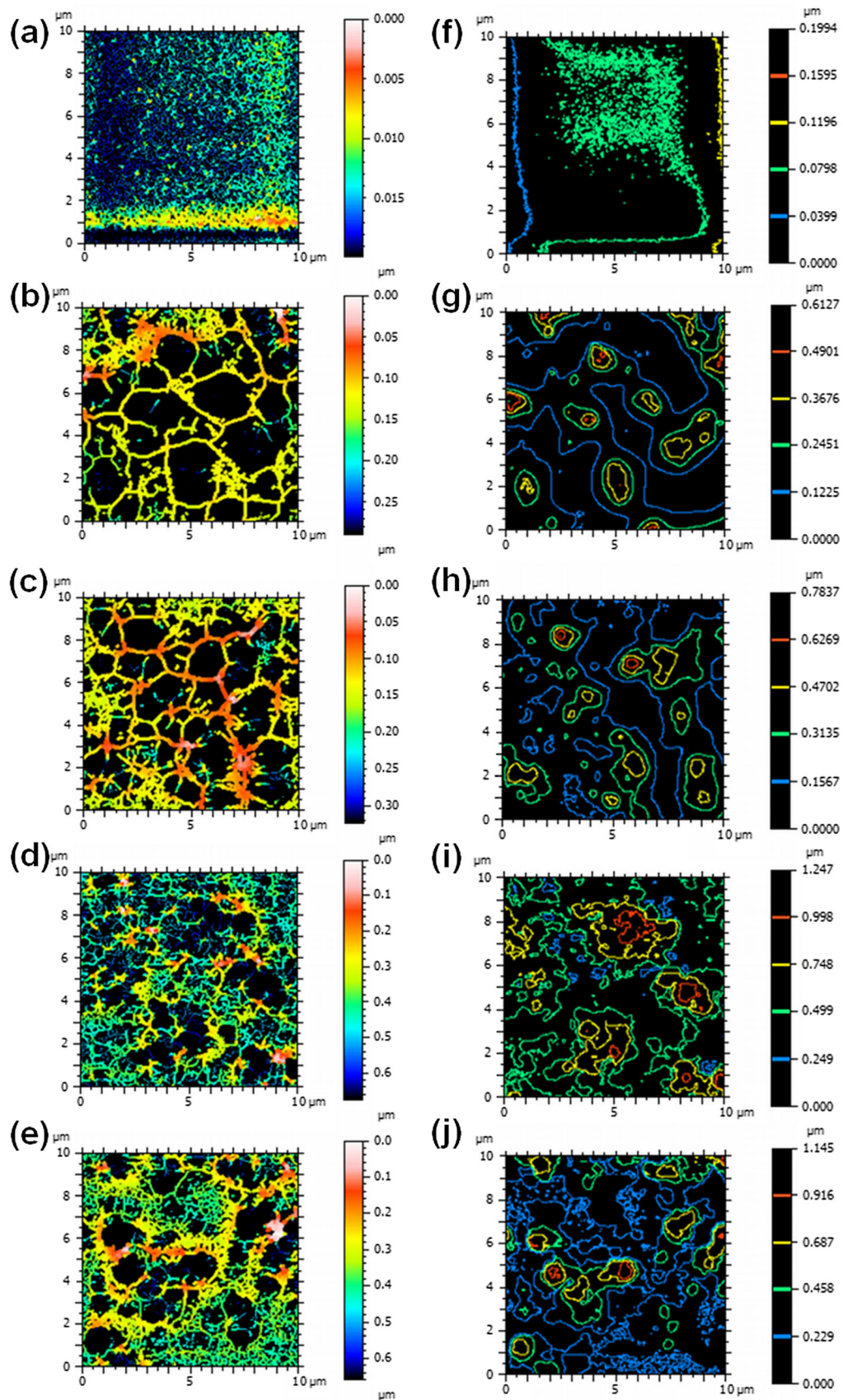


Fig. 4 Graphical representations of the furrows (#1 to #5 a–e) and lines contour (#1 to #5 f–j)

Table 2 Parameters of samples furrows

Furrows parameter	Samples				
	#1	#2	#3	#4	#5
Maximum depth (μm)	0.01914	0.2883	0.3050	0.6520	0.6573
Mean depth (μm)	0.005067	0.1521	0.1788	0.2445	0.2981
Mean density (cm/cm^2)	51,565	17,643	20,591	34,090	31,914

Probably, for minor cycles, a dynamic process occurred, while a static process was predominant for larger cycles.

Furthermore, in the second direction, the angles were random so that this direction did not provide information about the change in the texture of the thin films. However, the grain crystallization process was not complete, indicating that the texture of the films remained without completing their formation. Moreover, the more anisotropic behavior for higher cycles allowed evaluating the formation of the material texture.

Fractal parameters analysis

The fractal behavior of thin films was assessed using advanced fractal parameters. Many studies have reported that fractal theory can be a tool to evaluate the behavior of surface texture [72, 73, 75–81]. The data of these measurements are shown in Table 4.

The fractal dimension was performed by cube counting method and evaluated the texture homogeneity, as made in others works, e.g., [75, 82, 83]. The smallest measured fractal dimension was #1, while the largest was #4. However, all samples were similar. Therefore, this measure revealed a semiregular behavior of the surface texture. Therefore, the fractal dimension alone was not able to reveal which film had the most homogeneous surface texture.

All films also presented strong topographical uniformity, as H was found around 1 [84, 85]. The heights distribution was approximately homogeneous, as discussed for the superficial asymmetry, and the topographic uniformity to stabilize after #3, since the values for #4 and #5 were the same. When a surface exhibits H close to or equal to 1, the probability of discontinuity points is lower [55]. This is positive because the main problems related to corrosion or erosion of materials occur due to surface or structural failures. Therefore, there would be no points that allow flaws in the films, which was

Fig. 5 Representation of surface texture directions of the more relevant analyzed samples for **a** #1, **b** #2, **c** #3, **d** #4, and **e** #5

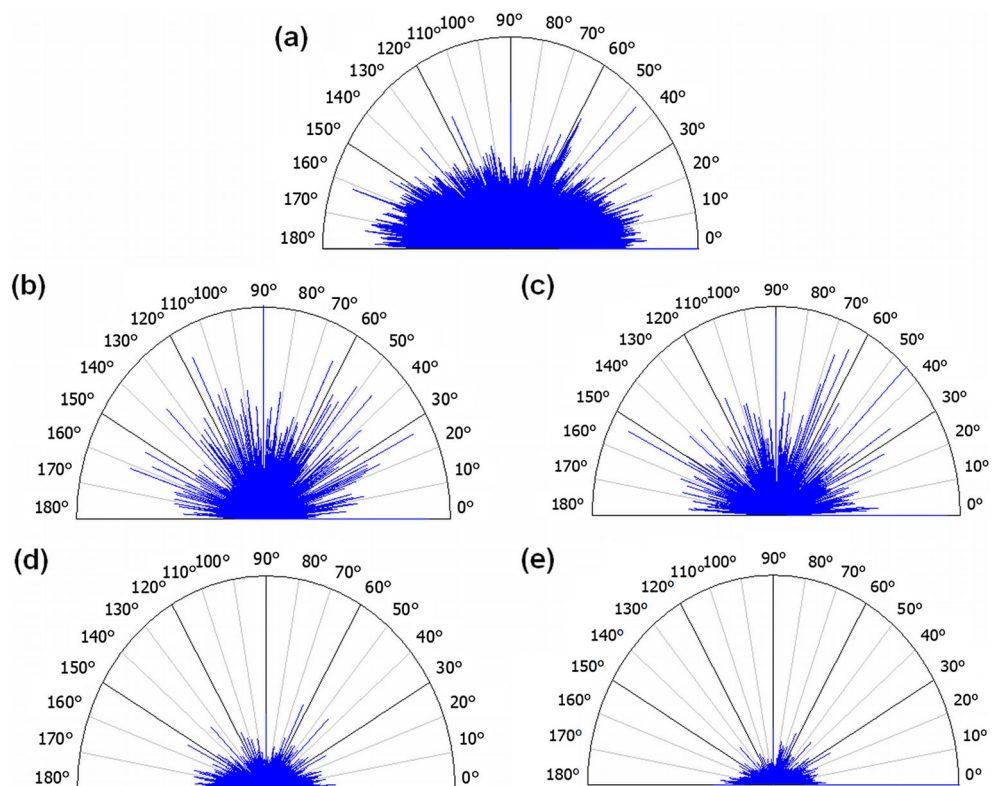


Table 3 Surface Texture Isotropy (STI) and their respective directions for more relevant analyzed samples

Sample	First direction (°)	Second direction (°)	Third direction (°)	STI (%)
#1	0.005959	45.02	161.5	17.81
#2	90	26.46	0.006748	86.28
#3	44.98	89.99	0.003731	83.29
#4	0.006948	45.02	153.5	67.51
#5	0.01703	26.49	44.99	72.71

also observed by Talu et al. [61]. However, it is still important to specifically evaluate the texture of the films. To obtain these responses, the percolation of the films was assessed by fractal succolarity and fractal lacunarity (Table 4).

According to Melo and Conci, the ideal fractal succolarity to have a good percolation is 0.5 [60]. The films presented values above 0.5. For the two largest cycles, this value was above 0.6, showing that the films presented an almost ideal percolation. These films were expected to exhibit this characteristic because they must be more resistant to the entrance of fluids, which may be corrosive. Additionally, the texture of the material is also dependent on these entrance directions because it can be affected by the erosion caused by corrosive agents. If the material has low percolation, it is more difficult for the texture to change. On the other hand, Fig. 6 revealed that the lacunarity decreased as a function of the box size for all samples. The films behave like a fractal object, presenting structures that are repeated along the surface, regardless of the scale. The highest value of the lacunarity coefficient was found in #1, while the lowest value occurred in #3. However, the most adjusted model for the lacunarity coefficient was observed for sample #5, as shown in Fig. 6e.

According to Salcedo et al. when β value is lower, the texture homogeneity is greater [62]. Moreover, Talu et al. state that when texture distribution is more uniform, the surface microtexture texture is also homogeneous [61]. This was observed in sample #3. Nevertheless, from # 3 to #5 the values remained in

the same decimal place, differing substrate #1 and film #2. For this reason, the film formation process homogenized the film’s texture. While the fractal dimension was not conclusive, the lacunarity quantitatively differentiated the surface microtexture of the films. Thus, as the number of cycles increased the texture of thin films, it became more homogeneous. We can attribute the homogenization of the surface texture to the increase in POEA conjugation for longer cycles. Probably, when the conjugation increased the energy difference between the representative molecular orbitals decreased, promoting a compaction of the structure and surface microtexture of POEA thin films. The main effect of this phenomenon was the closing of gaps in the surface, which allowed a greater homogenization of the surface texture.

Conclusions

In this work, we successfully synthesized POEA thin films by electrodeposition on the ITO substrate to evaluate morphology and texture using image processing. The molecular structure of thin films was studied using cyclic voltammetry and FTIR. The AFM technique was used to evaluate the morphology and microtexture of the thin films through topographic images. Image processing was performed using MountainsLab software. Molecular structure revealed the presence of absorption bands commonly associated to the POEA, whose polymer’s conjugation increased for longer cycles. The images revealed that the morphology of the films was affected by the number of cycles applied to the electrodeposition. Likewise, the microtexture changed when the number of cycles increased. The microtexture revealed more isotropic materials for smaller cycles and less isotropic materials for larger cycles. This behavior was associated with the incomplete grain coalescence process. Besides, new fractal parameters confirmed the change to microtexture, quantifying the topography uniformity and texture homogeneity. These new measurements used to characterize the texture presented interesting results.

Table 4 The results of Fractal Dimension FD, Topographic Entropy (H), Fractal Succolarity (FS), and Lacunarity Coefficient (β). The average results were expressed as mean value and standard deviation

Sample	FD	H	FS	β
#1	2.090 ± 0.008	0.96 ± 0.02	0.6 ± 0.1	0.0285
#2	2.130 ± 0.008	0.97 ± 0.04	0.6 ± 0.2	1.261e ⁻⁵
#3	2.13 ± 0.03	0.95 ± 0.04	0.6 ± 0.1	5.786e ⁻⁶
#4	2.25 ± 0.02	0.96 ± 0.05	0.63 ± 0.02	9.571e ⁻⁶
#5	2.23 ± 0.03	0.96 ± 0.04	0.7 ± 0.1	6.565e ⁻⁶

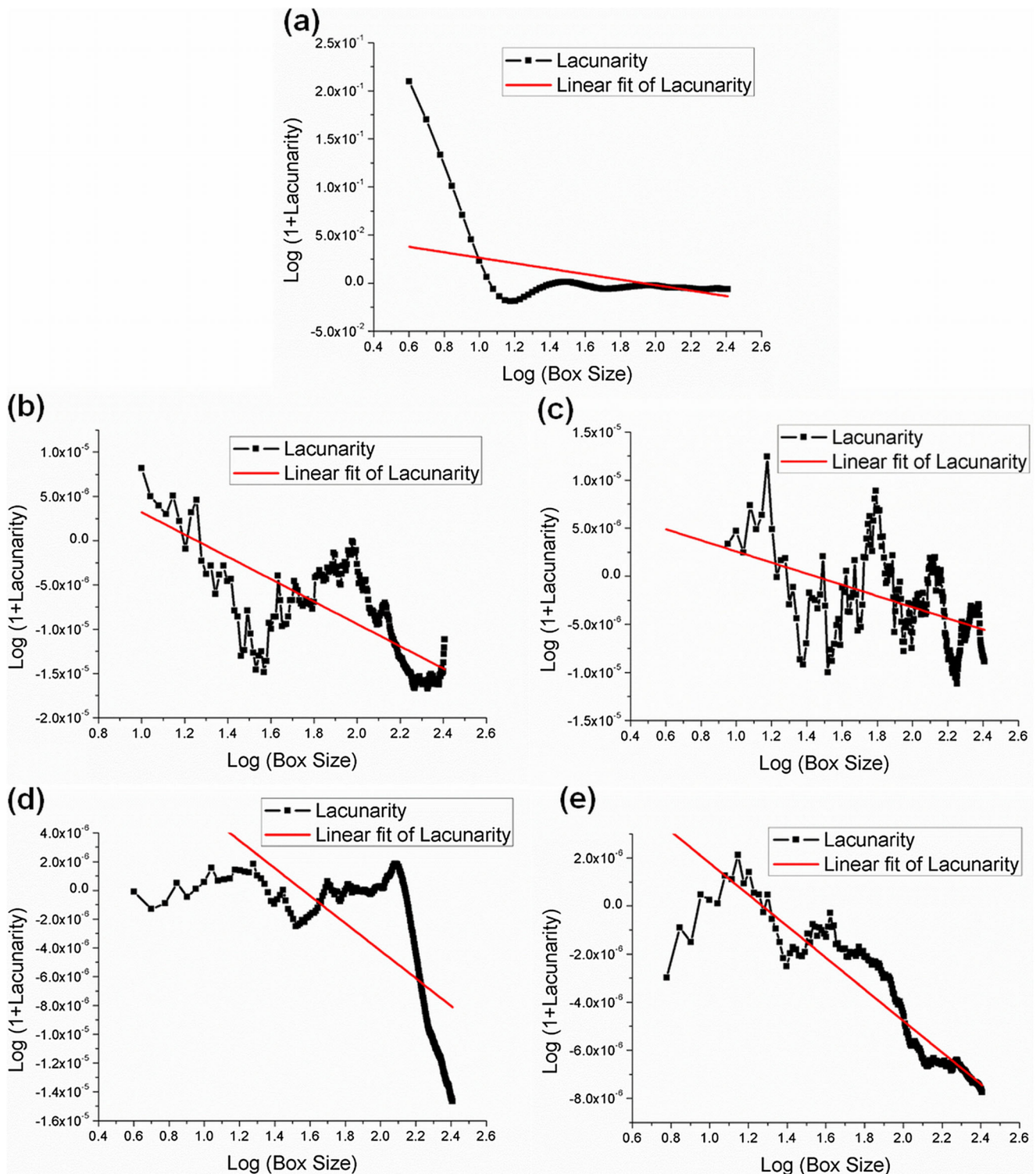


Fig. 6 Graphical representation of linear regression for the calculation of the lacunarity coefficient in **a** #1, **b** #2, **c** #3, **d** #4, and **e** #5

The fractal dimension was not enough to report conclusive results about texture, while fractal succolarity and lacunarity presented suitable results on the microtexture's homogeneity. Topographic entropy further revealed that the height distribution of all films

was uniform. These results revealed that these tools can be of great interest in the characterization of surfaces for technological application. They represent important information because the texture of POEA thin films is of great importance in the field of corrosion protection.

References

- Das TK, Prusty S (2012) Review on conducting polymers and their applications. *Polym Plast Technol Eng* 51:1487–1500. <https://doi.org/10.1080/03602559.2012.710697>
- Roković MK, Duić L (2006) Electrochemical synthesis of poly (ortho-ethoxyaniline) from phosphoric and sulphuric acid solutions. *Electrochim Acta* 51:6045–6050. <https://doi.org/10.1016/j.electacta.2005.12.052>
- Rajesh, Ahuja T, Kumar D (2009) Recent progress in the development of nano-structured conducting polymers/nanocomposites for sensor applications. *Sensors Actuators B Chem* 136:275–286. <https://doi.org/10.1016/j.snb.2008.09.014>
- Aydemir N, Malmström J, Travas-Sejdic J (2016) Conducting polymer based electrochemical biosensors. *Phys Chem Chem Phys* 18:8264–8277. <https://doi.org/10.1039/C5CP06830D>
- Moon J-M, Thapliyal N, Hussain KK, et al (2018) Conducting polymer-based electrochemical biosensors for neurotransmitters: a review. *Biosens Bioelectron* 102:540–552. <https://doi.org/10.1016/j.bios.2017.11.069>
- Zhao X, Liu Y, Lu J et al (2012) Temperature-responsive polymer/carbon nanotube hybrids: smart conductive Nanocomposite films for modulating the Bioelectrocatalysis of NADH. *Chem – A Eur J* 18:3687–3694. <https://doi.org/10.1002/chem.201103259>
- Zhou Q, Shi G (2016) Conducting polymer-based catalysts. *J Am Chem Soc* 138:2868–2876. <https://doi.org/10.1021/jacs.5b12474>
- Hou W, Xiao Y, Han G, Lin J-Y (2019) The applications of polymers in solar cells: a review. *Polymers (Basel)* 11:143. <https://doi.org/10.3390/polym11010143>
- Kim J, Lee J, You J et al (2016) Conductive polymers for next-generation energy storage systems: recent progress and new functions. *Mater Horizons* 3:517–535. <https://doi.org/10.1039/C6MH00165C>
- Gracia R, Mecerreyes D (2013) Polymers with redox properties: materials for batteries, biosensors and more. *Polym Chem* 4: 2206–2214. <https://doi.org/10.1039/C3PY21118E>
- Yuan L, Wan C, Ye X, Wu F (2016) Facial synthesis of silver-incorporated conductive polypyrrole submicron spheres for Supercapacitors. *Electrochim Acta* 213:115–123. <https://doi.org/10.1016/j.electacta.2016.06.165>
- Deshpande PP, Jadhav NG, Gelling VJ, Sazou D (2014) Conducting polymers for corrosion protection: a review. *J Coatings Technol Res* 11:473–494. <https://doi.org/10.1007/s11998-014-9586-7>
- Wu G, More KL, Johnston CM, Zelenay P (2011) High-performance electrocatalysts for oxygen reduction derived from polyaniline, iron, and cobalt. *Science* 80(332):443–447. <https://doi.org/10.1126/science.1200832>
- Bhadra J, Alkareem A, Al-Thani N (2020) A review of advances in the preparation and application of polyaniline based thermoset blends and composites. *J Polym Res* 27:122. <https://doi.org/10.1007/s10965-020-02052-1>
- Bilal S, Farooq S, Shah A-HA, Holze R (2014) Improved solubility, conductivity, thermal stability and corrosion protection properties of poly(o-toluidine) synthesized via chemical polymerization. *Synth Met* 197:144–153. <https://doi.org/10.1016/j.synthmet.2014.09.003>
- Sanches EA, Soares JC, Mafud AC et al (2013) Structural and morphological characterization of chloride salt of conducting poly(o-methoxyaniline) obtained at different time synthesis. *J Mol Struct* 1039:167–173. <https://doi.org/10.1016/j.molstruc.2012.12.025>
- Piza MA, Constantino CJL, Venancio EC, Mattoso LHC (2003) Interaction mechanism of poly (o-ethoxyaniline) and collagen blends. *Polymer (Guildf)* 44:5663–5670. [https://doi.org/10.1016/S0032-3861\(03\)00612-8](https://doi.org/10.1016/S0032-3861(03)00612-8)
- Paterno LG, Constantino CJL, Oliveira ON, Mattoso LHC (2002) Self-assembled films of poly(o-ethoxyaniline) complexed with sulfonated lignin. *Colloids Surf B Biointerfaces* 23:257–262. [https://doi.org/10.1016/S0927-7765\(01\)00266-1](https://doi.org/10.1016/S0927-7765(01)00266-1)
- Mattoso LHC, Manohar SK, Macdiarmid AG, Epstein AJ (1995) Studies on the chemical syntheses and on the characteristics of polyaniline derivatives. *J Polym Sci Part A Polym Chem* 33: 1227–1234. <https://doi.org/10.1002/pola.1995.080330805>
- Leite FL, Paterno LG, Borato CE et al (2005) Study on the adsorption of poly(o-ethoxyaniline) nanostructured films using atomic force microscopy. *Polymer (Guildf)*, 46:12503–12510. <https://doi.org/10.1016/j.polymer.2005.07.108>
- Leite FL, Borato CE, da Silva WTL, et al (2007) Atomic force spectroscopy on poly(o-ethoxyaniline) nanostructured films: sensing nonspecific interactions. *Microsc microanal* 13:304–312. /DOI: <https://doi.org/10.1017/S1431927607070262>
- Mello SV, Mattoso LHC, Santos JR et al (1995) Electrochemical response of poly(o-ethoxyaniline) films produced by different techniques. *Electrochim Acta* 40:1851–1855. [https://doi.org/10.1016/0013-4686\(95\)00130-7](https://doi.org/10.1016/0013-4686(95)00130-7)
- Amamath CA, Kim J, Kim K et al (2008) Nanoflakes to nanorods and nanospheres transition of selenious acid doped polyaniline. *Polymer (Guildf)* 49:432–437. <https://doi.org/10.1016/j.polymer.2007.12.005>
- Tran HD, D’Arcy JM, Wang Y et al (2011) The oxidation of aniline to produce “polyaniline”: a process yielding many different nano-scale structures. *J Mater Chem* 21:3534–3550. <https://doi.org/10.1039/C0JM02699A>
- Mello HJNPD, Mulato M (2018) Influence of galvanostatic electrodeposition parameters on the structure-property relationships of polyaniline thin films and their use as potentiometric and optical pH sensors. *Thin Solid Films* 656:14–21. <https://doi.org/10.1016/j.tsf.2018.04.022>
- Rohom AB, Londhe PU, Mahapatra SK et al (2014) Electropolymerization of polyaniline thin films. *High Perform Polym* 26:641–646. <https://doi.org/10.1177/0954008314538081>
- Wang H, Lin J, Shen ZX (2016) Polyaniline (PANI) based electrode materials for energy storage and conversion, *J Sci Adv Mater Devices*. 1:225–255. <https://doi.org/10.1016/j.jsamd.2016.08.001>
- Raghunathan A, Kahol PK, McCormick BJ (1999) Electron localization studies of alkoxy polyanilines. *Synth Met* 100:205–216. [https://doi.org/10.1016/S0379-6779\(99\)00008-9](https://doi.org/10.1016/S0379-6779(99)00008-9)
- Chaudhari S, Patil PP (2007) Corrosion protective poly(o-ethoxyaniline) coatings on copper. *Electrochim Acta* 53:927–933. <https://doi.org/10.1016/j.electacta.2007.08.002>
- Shinde V, Patil PP (2010) Evaluation of corrosion protection performance of poly(o-ethyl aniline) coated copper by electrochemical impedance spectroscopy. *Mater Sci Eng B* 168:142–150. <https://doi.org/10.1016/j.mseb.2009.11.008>
- Shinde VP (2018) Study of water transport characteristics of poly(o-ethyl aniline) coatings: corrosion mechanism. *Ionics (Kiel)* 24:605–615. <https://doi.org/10.1007/s11581-017-2213-8>
- Cena CR, Malmonge LF, Malmonge JA (2017) Layer-by-layer thin films of polyaniline alternated with natural rubber and their potential application as a chemical sensor. *J Polym Res* 24:1–7. <https://doi.org/10.1007/s10965-016-1170-7>
- Raoufi D, Hosseinpanahi F, Raoufi D, Hosseinpanahi F (2012) Surface morphology dynamics in ITO thin films. *J Mod Phys* 03: 645–651. <https://doi.org/10.4236/jmp.2012.38088>
- Schmahling J (2006) Statistical characterization of technical surface microstructure
- Sayyad Amin J, Nikoee E, Ayatollahi S, Alamdari A (2010) Investigating wettability alteration due to asphaltene precipitation:

- imprints in surface multifractal characteristics. *Appl Surf Sci* 256: 6466–6472. <https://doi.org/10.1016/j.apsusc.2010.04.036>
36. Dallaeva D, Tălu Ş, Stach S et al (2014) AFM imaging and fractal analysis of surface roughness of AlN epilayers on sapphire substrates. *Appl Surf Sci* 312:81–86. <https://doi.org/10.1016/j.apsusc.2014.05.086>
 37. Vilt SG, Caswell CJ, Tuberquia JC et al (2012) Effect of roughness on the microscale friction of hydrocarbon films. *J Phys Chem C* 116:21795–21801. <https://doi.org/10.1021/jp305527h>
 38. Xu L, Karunakaran RG, Guo J, Yang S (2012) Transparent, Superhydrophobic surfaces from one-step spin coating of hydrophobic nanoparticles. *ACS Appl Mater Interfaces* 4:1118–1125. <https://doi.org/10.1021/am201750h>
 39. Cho KL, Liaw II, Wu AH-F, Lamb RN (2010) Influence of roughness on a transparent superhydrophobic coating. *J Phys Chem C* 114:11228–11233. <https://doi.org/10.1021/jp103479k>
 40. Sedlaček M, Podgornik B, Vižintin J (2012) Correlation between standard roughness parameters skewness and kurtosis and tribological behaviour of contact surfaces. *Tribol Int* 48:102–112. <https://doi.org/10.1016/j.triboint.2011.11.008>
 41. Gong Y, Mixture ST, Gao P, Mellott NP (2016) Surface roughness measurements using power spectrum density analysis with enhanced spatial correlation length. *J Phys Chem C* 120:22358–22364. <https://doi.org/10.1021/acs.jpcc.6b06635>
 42. Senthilkumar M, Sahoo NK, Thakur S, Tokas RB (2005) Characterization of microroughness parameters in gadolinium oxide thin films: a study based on extended power spectral density analyses. *Appl Surf Sci* 252:1608–1619. <https://doi.org/10.1016/j.apsusc.2005.02.122>
 43. Yuan CQ, Li J, Yan XP, Peng Z (2003) The use of the fractal description to characterize engineering surfaces and wear particles. *Wear* 255:315–326. [https://doi.org/10.1016/S0043-1648\(03\)00206-0](https://doi.org/10.1016/S0043-1648(03)00206-0)
 44. Yadav RP, Dwivedi S, Mittal AK et al (2012) Fractal and multifractal analysis of LiF thin film surface. *Appl Surf Sci* 261: 547–553. <https://doi.org/10.1016/j.apsusc.2012.08.053>
 45. Yadav RP, Kumar M, Mittal AK, Pandey AC (2015) Fractal and multifractal characteristics of swift heavy ion induced self-affine nanostructured BaF₂ thin film surfaces. *Chaos An Interdiscip J Nonlinear Sci* 25:083115. <https://doi.org/10.1063/1.4928695>
 46. Mandelbrot BB, Wheeler JA (1983) The fractal geometry of nature. *Am J Phys* 51:286–287. <https://doi.org/10.1119/1.13295>
 47. Consolin Filho N, de Leite FL, Carvalho ER et al (2007) Study of poly(o-Ethoxyaniline) interactions with herbicides and evaluation of conductive polymer potential used in electrochemical sensors. *J Braz Chem Soc* 18:577–584. <https://doi.org/10.1590/S0103-50532007000300013>
 48. Leite FL, de Oliveira NM, Paterno LG et al (2007) Nanoscale conformational ordering in polyanilines investigated by SAXS and AFM. *J Colloid Interface Sci* 316:376–387. <https://doi.org/10.1016/j.jcis.2007.08.069>
 49. de Sousa FDB, Scuracchio CH (2014) The use of atomic force microscopy as an important technique to analyze the dispersion of nanometric fillers and morphology in nanocomposites and polymer blends based on elastomers. *Polímeros* 24:661–672. <https://doi.org/10.1590/0104-1428.1648>
 50. Silva-Moraes MO, Garcia-Basabe Y, de Souza RFB et al (2018) Geometry-dependent DNA-TiO₂ immobilization mechanism: a spectroscopic approach. *Spectrochim Acta Part A Mol Biomol Spectrosc* 199:349–355. <https://doi.org/10.1016/J.SAA.2018.03.081>
 51. Digital Surf - Surface Imaging, Analysis and Metrology Software
 52. (2012) ISO – ISO 25178-2:2012 – Geometrical product specifications (GPS)—Surface texture: Areal—Part 2: Terms, definitions and surface texture parameters. <https://www.iso.org/standard/42785.html>. Accessed 11 May 2020
 53. Horcas I, Fernández R, Gómez-Rodríguez JM et al (2007) WSXM: a software for scanning probe microscopy and a tool for nanotechnology. *Rev Sci Instrum* 78:013705. <https://doi.org/10.1063/1.2432410>
 54. Khulbe KC, Feng CY, Matsuura T (2008) Synthetic polymeric membranes. 1st. edn. Springer, Berlin
 55. Matos RS, Lopes GAC, Ferreira NS et al (2018) Superficial characterization of kefir biofilms associated with Açai and Cupuaçu extracts. *Arab J Sci Eng* 43:3371–3379. <https://doi.org/10.1007/s13369-017-3024-y>
 56. Nosonovsky M (2010) Entropy in tribology: in the search for applications. *Entropy* 12:1345–1390. <https://doi.org/10.3390/e12061345>
 57. Citing RStudio, RStudio Support
 58. Henebry GM, Kux HJH (1995) Lacunarity as a texture measure for SAR imagery. *Int J Remote Sens* 16:565–571. <https://doi.org/10.1080/01431169508954422>
 59. Nečas D, Klapetek P (2012) Gwyddion: an open-source software for SPM data analysis. *Cent Eur J Phys* 10:181–188. <https://doi.org/10.2478/s11534-011-0096-2>
 60. de Melo RHC, Conci A (2008) Succolarity: defining a method to calculate this fractal measure. In: 2008 15th international conference on systems, Signals and Image Processing. IEEE, pp. 291–294
 61. Tălu Ş, Abdolghaderi S, Pinto EP et al (2020) Advanced fractal analysis of nanoscale topography of Ag/DLC composite synthesized by RF-PECVD. *Surf Eng* 36:713–719. <https://doi.org/10.1080/02670844.2019.1710937>
 62. Omar M, Salcedo C, Ronald R et al (2016) Study fractal leaf surface of the plant species *Copaifera* sp. using the microscope atomic-force-AFM. *Rev ECIPerú* 13:10–16. <https://doi.org/10.33017/RevECIPerú2016.0002/>
 63. Oreški S (2012) Programsko okolje Force 3.0 : kratek priročnik za uporabo. Fakulteta za kemijo in kemijsko tehnologijo
 64. de Lucena LRR, Xavier Junior SF, Stosic T, Stosic B (2018) Lacunarity analysis of daily rainfall data in Pernambuco, Brazil. *Acta Sci Technol* 40:36655. <https://doi.org/10.4025/actascitechnol.v40i1.36655>
 65. Silva AS, Soares JC, Carolina A et al (2014) Structural and morphological characterization of Poly(o-ethoxyaniline) Emeraldine-salt form using FTIR, XRD, LeBail Method and SEM. *J Mol Struct*. <https://doi.org/10.1016/j.molstruc.2014.04.039>
 66. Noppakuadritidej P, Vailikhit V, Teesetsopon P et al (2018) Copper incorporation in Mn²⁺-doped Sn₂S₃ nanocrystals and the resultant structural, optical, and electrochemical characteristics. *Ceram Int* 44:13973–13985. <https://doi.org/10.1016/j.ceramint.2018.04.247>
 67. Leite FL, Alves WF, Mir M et al (2008) TEM, XRD and AFM study of poly(o-ethoxyaniline) films: new evidence for the formation of conducting islands. *Appl Phys A* 93:537. <https://doi.org/10.1007/s00339-008-4686-9>
 68. Chihai A, Bessais B (2017) Characterization and photoelectrochemical properties of CICS thin films grown via an electrodeposition route. *RSC Adv* 7:29469–29480. <https://doi.org/10.1039/C7RA04330A>
 69. Aydın M, Aydın EB, Sezgintürk MK (2018) A disposable immunosensor using ITO based electrode modified by a star-shaped polymer for analysis of tumor suppressor protein p53 in human serum. *Biosens Bioelectron* 107:1–9. <https://doi.org/10.1016/j.bios.2018.02.017>
 70. Aydın EB, Aydın M, Sezgintürk MK (2018) Electrochemical immunosensor based on chitosan/conductive carbon black composite modified disposable ITO electrode: an analytical platform for p53 detection. *Biosens Bioelectron* 121:80–89. <https://doi.org/10.1016/j.bios.2018.09.008>
 71. Matos RS, Pinto EP, Ramos GQ, et al (2020) Stereometric characterization of kefir microbial films associated with *Maytenus rigida*

- extract. *Microsc Res Tech Jemt* 23532. <https://doi.org/10.1002/jemt.23532>
72. ȃlu Œ, Ghaderi A, StepieŒ K, Mwema FM (2019) Advanced micromorphology analysis of cu/Fe NPs thin films. *IOP Conf Ser Mater Sci Eng* 611:012016. <https://doi.org/10.1088/1757-899X/611/1/012016>
 73. Ansari F, Granda LA, Joffe R et al (2017) Experimental evaluation of anisotropy in injection molded polypropylene/wood fiber biocomposites. *Compos Part A Appl Sci Manuf* 96:147–154. <https://doi.org/10.1016/j.compositesa.2017.02.003>
 74. Heshmati V, Zolali AM, Favis BD (2017) Morphology development in poly (lactic acid)/polyamide11 biobased blends: chain mobility and interfacial interactions. *Polymer (Guildf)* 120:197–208. <https://doi.org/10.1016/j.polymer.2017.05.056>
 75. Arman A, ȃlu Œ, Luna C et al (2015) Micromorphology characterization of copper thin films by AFM and fractal analysis. *J Mater Sci Mater Electron* 26:9630–9639. <https://doi.org/10.1007/s10854-015-3628-5>
 76. Jing C, Tang W (2016) Ga-doped ZnO thin film surface characterization by wavelet and fractal analysis. *Appl Surf Sci* 364:843–849. <https://doi.org/10.1016/j.apsusc.2015.12.234>
 77. Yadav RP, Kumar T, Baranwal V et al (2017) Fractal characterization and wettability of ion treated silicon surfaces. *J Appl Phys* 121: 055301. <https://doi.org/10.1063/1.4975115>
 78. Astinchap B (2019) Fractal and statistical characterization of Ti thin films deposited by RF-magnetron sputtering: the effects of deposition time. *Optik (Stuttg)* 178:231–242. <https://doi.org/10.1016/j.ijleo.2018.10.050>
 79. Shakoury R, Rezaee S, Mwema F et al (2020) Multifractal and optical bandgap characterization of Ta2O5 thin films deposited by electron gun method. *Opt Quantum Electron* 52. <https://doi.org/10.1007/s11082-019-2173-5>
 80. ȃlu Œ, Patra N, Salerno M (2015) Micromorphological characterization of polymer-oxide nanocomposite thin films by atomic force microscopy and fractal geometry analysis. In: *Progress in Organic Coatings*. Elsevier, pp. 50–56
 81. ȃlu Œ, Bramowicz M, Kulesza S, Solaymani S (2018) Topographic characterization of thin film field-effect transistors of 2,6-diphenyl anthracene (DPA) by fractal and AFM analysis. *Mater Sci Semicond Process* 79:144–152. <https://doi.org/10.1016/j.mssp.2018.02.008>
 82. Sobola D, Talu S, Sadovsky P et al (2017) Application of afm measurement and fractal analysis to study the surface of natural optical structures. *Adv Electr Electron Eng* 15:569–576. <https://doi.org/10.15598/aeec.v15i3.2242>
 83. Sobola D, ȃlu Œ, Solaymani S, Grmela L (2017) Influence of scanning rate on quality of AFM image: study of surface statistical metrics. *Microsc Res Tech* 80:1328–1336. <https://doi.org/10.1002/jemt.22945>
 84. Matos RS, Ramos GQ, da Fonseca Filho HD, ȃlu Œ (2020) Advanced micromorphology study of microbial films grown on kefir loaded with Açaí extract. *Micron*. <https://doi.org/10.1016/j.micron.2020.102912>
 85. de Oliveira LM, Matos RS, Campelo PH et al (2020) Evaluation of the nanoscale surface applied to biodegradable nanoparticles containing Allium sativum essential oil. *Mater Lett* 275:128111. <https://doi.org/10.1016/j.matlet.2020.128111>

Publisher's note Springer Nature remains neutral with regard to jurisdictional claims in published maps and institutional affiliations.